JOURNAL OF SYNCHROTRON RADIATION
ISSN 1600-5775

X-ray fluorescence induced by standing waves in the grazing-incidence and grazing-exit modes: study of the Mg–Co–Zr system

Yuchun Tu,[a,b,c]‡ Yanyan Yuan,[a,b]§ Karine Le Guen,[a,b] Jean-Michel André,[a,b] Jingtao Zhu,[c] Zhanshan Wang,[c] Françoise Bridou,[d] Angelo Giglia[e] and Philippe Jonnard[a,b]*

[a]Sorbonne Universités, UPMC Université Paris 06, Laboratoire de Chimie Physique – Matière et Rayonnement, 11 Rue Pierre et Marie Curie, F-75231 Paris Cedex 05, France, [b]CNRS UMR 7614, Laboratoire de Chimie Physique – Matière et Rayonnement, 11 Rue Pierre et Marie Curie, F-75231 Paris Cedex 05, France, [c]MOE Key Laboratory of Advanced Micro-structured Materials, School of Physics Science and Engineering, Tongji University, Shanghai 200092, People's Republic of China, [d]Laboratoire Charles Fabry, Institut d'Optique, CNRS UMR 8501, Université Paris Sud 11, 2 Avenue Augustin Fresnel, F-91127 Palaiseau Cedex, France, and [e]CNR-Istituto Officina Materiali, I-34149 Trieste, Italy. *Correspondence e-mail: philippe.jonnard@upmc.fr

Received 8 April 2015
Accepted 31 August 2015

Edited by A. Momose, Tohoku University, Japan

‡ On leave from Shanghai Institute of Laser Plasma, People's Republic of China.
§ On leave from Jiangsu University of Science and Technology, People's Republic of China.

Keywords: X-ray standing wave; X-ray fluorescence; multilayer; interface.

The characterization of Mg–Co–Zr tri-layer stacks using X-ray fluorescence induced by X-ray standing waves, in both the grazing-incidence (GI) and the grazing-exit (GE) modes, is presented. The introduction of a slit in the direction of the detector improves the angular resolution by a factor of two and significantly improves the sensitivity of the technique for the chemical characterization of the buried interfaces. By observing the intensity variations of the Mg $K\alpha$ and Co $L\alpha$ characteristic emissions as a function of the incident (GI mode) or detection (GE mode) angle, it is shown that the interfaces of the Si/[Mg/Co/Zr]$_{\times 30}$ multilayer are abrupt, whereas in the Si/[Mg/Zr/Co]$_{\times 30}$ multilayer a strong intermixing occurs at the Co-on-Zr interfaces. An explanation of this opposite behavior of the Co-on-Zr and Zr-on-Co interfaces is given by the calculation of the mixing enthalpies of the Co–Mg, Co–Zr and Mg–Zr systems, which shows that the Co–Zr system presents a negative value and the other two systems present positive values. Together with the difference of the surface free energies of Zr and Co, this leads to the Mg/Zr/Co system being considered as a Mg/Co$_x$Zr$_y$ bi-layer stack, with x/y estimated around 3.5.

1. Introduction

Periodic multilayers alternating two or more layers of nanometer thickness can be used to diffract radiation in the X-ray and extreme ultraviolet ranges (Attwood, 2000). Thus, they are used as optical components for numerous applications in photolithography, X-ray microscopy, X-ray spectroscopy, in space telescopes or on synchrotron beamlines. However, the optical performance of such multilayer stacks greatly depends on the quality of their interfaces. So it is important to characterize them, which is often done by X-ray reflectivity in the hard X-ray range or at the application wavelength or by transmission electron microscopy.

Recently we have demonstrated (Jonnard *et al.*, 2014) that X-ray fluorescence (XRF) generated by X-ray standing waves (XSW), combining both grazing-incidence (GI) and grazing-exit (GE) modes, is an efficient means for the characterization of such stacks. Indeed, the standing wave generated by the incident radiation (GI mode) or characteristic emission (GE mode) has the same period as the multilayer. Then, by rotating the sample in an angular range centered around the Bragg

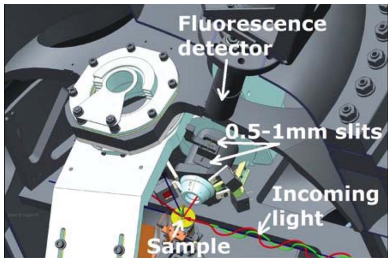

angle of the incident or emitted radiation, it is possible to move the nodes and anti-nodes of the electric field at specific positions within the stack, an interface or the center of a layer, and thus to locate the origin of the generated X-ray signal with great depth sensitivity (Bedzyk & Libera, 2013). This technique is related to the technique of XSW at grazing incidence and grazing exit (Sakata & Jach, 2013).

We apply GI-XRF and GE-XRF to the Mg–Co–Zr tri-layer system whose period thickness, around 9.5 nm, was designed to have constructive interferences and a Bragg peak at not extreme grazing incidence. Two tri-layers, Si/[Mg/Co/Zr]$_{\times 30}$ and Si/[Mg/Zr/Co]$_{\times 30}$, were deposited by magnetron sputtering, where the order of the layers in the stack is different. This kind of multilayer system had already been studied for optical applications around the 25 nm spectral range (Le Guen *et al.*, 2011*a*,*b*). With respect to the present multilayers, the Co and Zr thicknesses were the same whereas the Mg layers were much thicker. They have been thoroughly characterized by X-ray reflectivity in the hard and soft X-ray ranges, X-ray emission spectroscopy, nuclear magnetic resonance spectroscopy, secondary ion mass spectrometry and also transmission electron microscopy (Le Guen *et al.*, 2011*a*,*b*; Zhu *et al.*, 2011; Jonnard *et al.*, 2013).

This paper is organized as follows. Firstly, in the experimental section we indicate how the samples are prepared and recall some details of the GI- and GE-XRF experiments. We present the improvement of the angular resolution in the GE mode with respect to our previous study of the Co/Mg bi-layer system. The way simulations are obtained and handled for comparison with the experimental curves is then described. Finally, we present and discuss comparatively the results for both tri-layer systems, obtained in the GI and GE modes, giving the angular variations of the intensity of the Mg $K\alpha$ ($2p$–$1s$ transition) and Co $L\alpha$ ($3d$–$2p_{3/2}$ transition) characteristic emissions.

2. Experimental methods

2.1. Samples

The deposition of the samples was carried out using magnetron sputtering onto silicon wafers used as substrates. After deposition, a 3.5 nm-thick boron carbide (B_4C) thin layer was added as a capping layer to prevent the oxidation of the samples. Different multilayers were deposited on the basis of the Si/[Mg (5.45 nm)/Co (2.45 nm)]$_{30}$/B_4C (3.5 nm) bi-layer system. The Mg/Co bi-layer system has already been studied using GI- and GE-XRF (Jonnard *et al.*, 2014) and is used here for the purpose of demonstrating an improvement in the angular resolution and to reveal that a combination of both the GI and GE modes is a powerful method for the characterization of buried interfaces of already very well studied systems. The two tri-layer samples are:

(*a*) Si/[Mg (5.45 nm)/Co (2.45 nm)/Zr (1.50 nm)]$_{30}$/B_4C (3.5 nm), denoted as Mg/Co/Zr;

(*b*) Si/[Mg (5.45 nm)/Zr (1.50 nm)/Co (2.45 nm)]$_{30}$/B_4C (3.5 nm), denoted as Mg/Zr/Co.

Table 1
Parameters of the tri-layer systems as deduced from the fits of their reflectivity curves.

For each layer, its thickness (nm), density (g cm^{-3}) and interface width (nm) are indicated.

Sample	Period (nm)	Mg	Co	Zr
Mg/Co/Zr	9.45	5.22/1.6/0.5	2.61/8.8/0.5	1.62/6.5/0.6
Mg/Zr/Co	9.57	5.49/1.6/0.5	2.35/8.8/0.5	1.73/6.5/0.6

With this notation the layers are written in the order of their deposition.

Following deposition, all the samples were characterized by grazing-incidence X-ray reflectivity at the Cu $K\alpha$ wavelength (0.154 nm). The thickness, roughness and density of each layer were determined by fitting the reflectivity curves using the designed one as a model of the stack. The results are given in Table 1 for the tri-layer systems. The stack parameters are close to the designed ones. The roughness, or interface width, is limited to around 0.5 nm.

2.2. Schemes of the experiments

The experimental details have already been given (Jonnard *et al.*, 2014) and here we only recall the main characteristics of our two experimental procedures, both performed on the same samples. Experiments were performed at the BEAR beamline of the ELETTRA synchrotron radiation facility (Nannarone *et al.*, 2004). Prior to the XSW experiments, we obtained an XRF spectrum of one sample with a silicon drift detector (SDD) to determine in which spectral region the fluorescence emission of an element, Co $L\alpha$ or Mg $K\alpha$ in our case, should be integrated. The incident photon energy to excite the Co $L\alpha$ emission was 807.6 eV; it was 1332 eV to excite the Mg $K\alpha$ emission.

In the GI-XRF mode, the intensity of an emission is measured as a function of the glancing angle i, *i.e.* the angle between the synchrotron beam and the sample surface, for angles close to the Bragg angle calculated from the period of the sample and the wavelength of the incident radiation. In the GE-XRF mode, the intensity of an emission is measured as a function of the take-off angle of emission d, *i.e.* the angle between the detector and the sample surface, for angles close to the Bragg angle calculated from the period of the sample and the wavelength of the characteristic emitted radiation. This is illustrated in Fig. 1. In our case there is a fixed angle of 60° between the directions of the incident and the detected radiations. From this mechanical constraint, $d = 120 - i$ (angles in degrees). In both modes, the SDD is located in the incidence plane, *i.e.* the plane defined by the incident beam and the normal to the sample surface.

2.3. Angular resolution in GE-XRF mode

In GI-XRF the angular resolution is governed by the divergence of the incident beam, that is to say of the synchrotron radiation beam. It is quite small, 0.2° under our

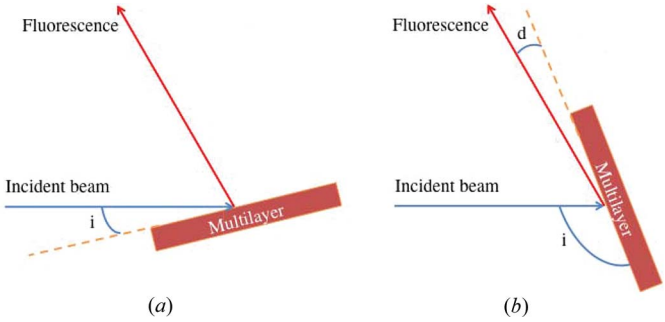

Figure 1
Experimental configurations for the GI-XRF (*a*) and GE-XRF (*b*) experiments, where *i* is the glancing angle and *d* is the glancing take-off angle.

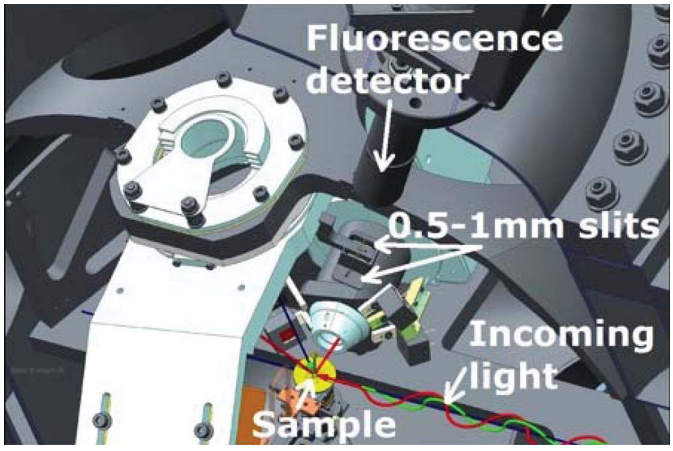

Figure 2
Experimental setup. The slit holder can be rotated to put one of the two narrow slits in the axis going from the sample to the detector.

experimental conditions. In GE-XRF the angular resolution is governed by the aperture of the detector. Taking into account the aperture of the SDD, 5 mm, and its distance from the sample, 300 mm, leads to a 0.9° angular aperture. As shown in Fig. 2, in order to improve the angular resolution we can insert two slits with widths of 1.0 or 0.5 mm, at 140 mm from the sample and 160 mm from the SDD. These configurations correspond to angular acceptances of 0.4 and 0.2°, respectively. The rotation of the slit holder around the azimuthal axis allows the desired slit to be put in the incidence plane.

We present in Fig. 3 the GE-XRF curves showing the variations of the Mg *Kα* intensity of the Co/Mg sample with three possible configurations to check the angular resolution: without slit and with a slit of 1.0 mm and 0.5 mm. In all three cases the main feature around 3°, relative to the first-order diffraction of the emitted radiation, is clearly observed. However, the feature regarding the second-order diffraction of the emitted radiation, located around 6°, is hardly seen without a slit and is better distinguished when the slit width decreases. This is due to the improvement of the angular resolution, as can be seen on the normalized curves (Fig. 3*b*). We estimate to have gained a factor of two on the resolution when going from the configuration with no slit to that with the 0.5 mm slit. This was estimated from the angular distance between the maximum and the dip of the first-order feature. Let us note that the improvement of the resolution is detrimental to the collected intensity, which decreases by a factor of three, as can be seen in the raw data (Fig. 3*a*). However, owing to the large incident flux delivered by the synchrotron, we choose in the following to work in the configuration with the narrowest slit.

2.4. Fit of the experimental curves

The fit of the experiment relies on simulations of the intensity of the characteristic fluorescence radiation. As the model has already been presented (Chauvineau & Bridou, 1996; Jonnard *et al.*, 2014), we recall only its main points. First, the intensity of the exciting electromagnetic field at a given depth in the stack and below a given glancing angle *i* is calculated. This is done from the recurrent formalism used to calculate the optical properties of stacks from the optical constants and thicknesses of its various layers. The intensity generated at the same depth from an element of a given concentration is proportional to the square of the electric field and to the concentration. Then, the fluorescence intensity arriving below the take-off angle *d* from the source to be located is calculated by applying the reciprocity theorem (von Laue, 1935; James, 1962). Let us note that the chosen formalism can be applied to both GI and GE modes. Thus, the fits are performed so that a best agreement is obtained for both GI and GE curves at the same time. This imposes a strict constraint on the fitted parameters. They are the same as those determined from the reflectivity measurements (thickness, roughness and density of the layers), which are generally used as input values. The roughness of the various layers is intro-

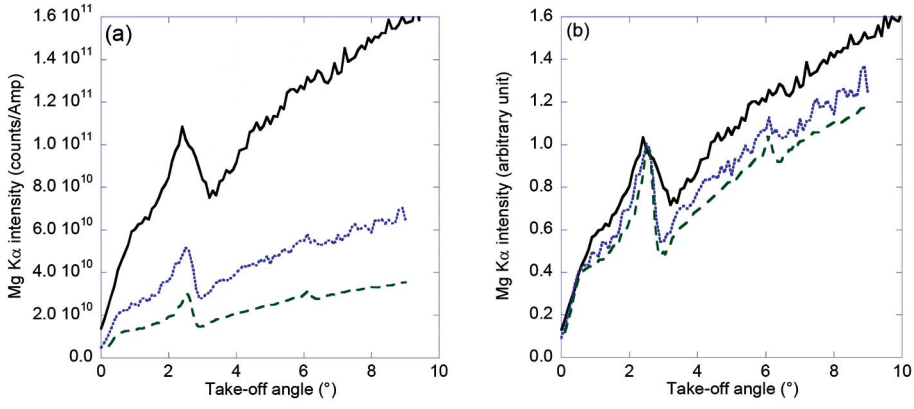

Figure 3
GE-XRF of the Mg *Kα* emission of the Co/Mg sample: (*a*) raw data and (*b*) data normalized to the maximum of the first diffraction order feature. Measurement with no detection slit (solid line), with a 1.0 mm slit (dotted line) and with a 0.5 mm slit (dashed line).

duced and considered fixed at the value given by the reflectivity measurement. The boron carbide capping layer is also considered with its nominal thickness.

To compare properly the experimental and simulated curves requires the effect of the beam imprint on the sample to be taken into account. Indeed, contrary to the case of reflectivity measurements where the specular geometry ensures that the imprint of the incident and reflected beams is the same, this is not the case for GE and GI measurements owing to the asymmetric geometry. Thus in the GI case, a $1/\sin(i)$ factor (Li *et al.*, 2012) is introduced. For the GE mode, no geometrical factor was taken into account because this correction is significant only for the small glancing angles. The simulated curves are then normalized on one point of the experimental curve.

3. Results and discussion

For both Mg $K\alpha$ and Co $L\alpha$ emissions, we show in Figs. 4 and 5 the GI- and GE-XRF curves of the Mg/Co/Zr and Mg/Zr/Co multilayers, respectively. The modulation of the intensity is clearly observed on each curve at an angle close to that calculated from the Bragg law at the first and second diffraction orders. It can be seen that the amplitudes of the observed features are quite similar in the case of the Mg $K\alpha$ emission of both samples, whereas for the Co $L\alpha$ emission the features exhibit a higher contrast for Mg/Co/Zr [Figs. 4(*c*) and 4(*d*)] with respect to those of Mg/Zr/Co [Figs. 5(*c*) and 5(*d*)]. This is valid for both GI and GE modes and can be seen in Figs. 6(*a*) and 6(*b*) where the experimental XSW curves of the Mg/Co/Zr and Mg/Zr/Co multilayers are compared.

The simulation of the Mg $K\alpha$ emission of Mg/Co/Zr and Mg/Zr/Co multilayers is carried out with the parameters deduced from the reflectivity measurements, thus considering a tri-layer stack. We can deduce that in these multilayers the interfaces involving the Mg layers, Mg–Co and Mg–Zr, are abrupt. This is in agreement with previous results (Le Guen *et al.*, 2011*a*,*b*; Zhu *et al.*, 2011) of

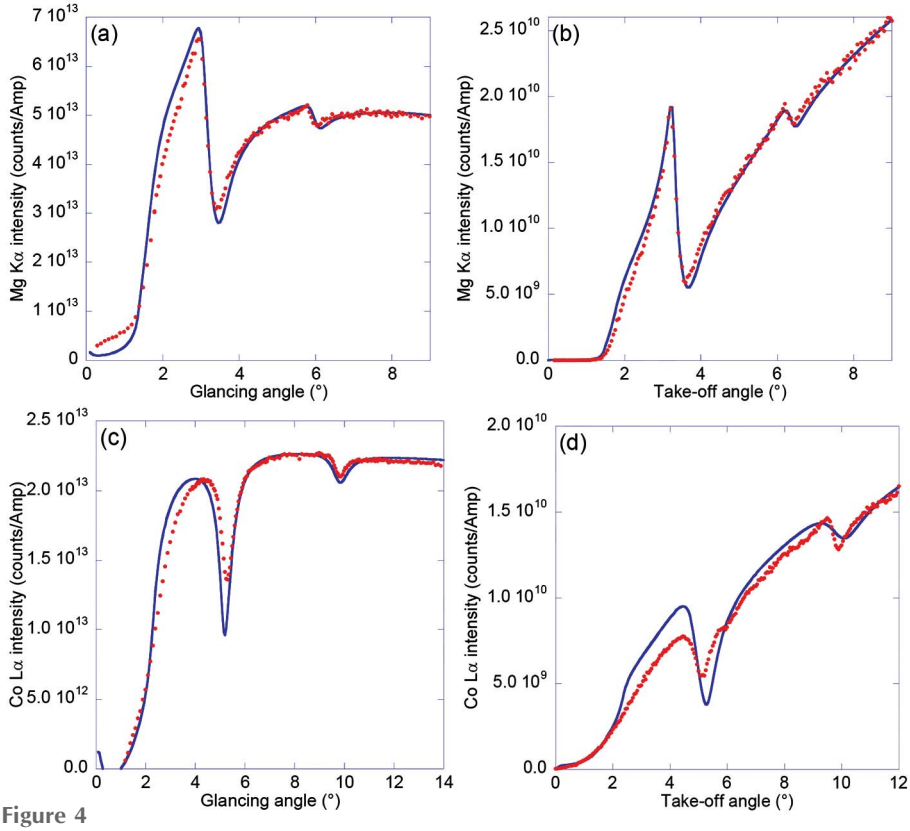

Figure 4
GI-XRF (*a*, *c*) and GE-XRF (*b*, *d*) curves for the Mg $K\alpha$ (*a*, *b*) and Co $L\alpha$ (*c*, *d*) emissions of the Mg/Co/Zr multilayer: dots, experiment; solid line: fit.

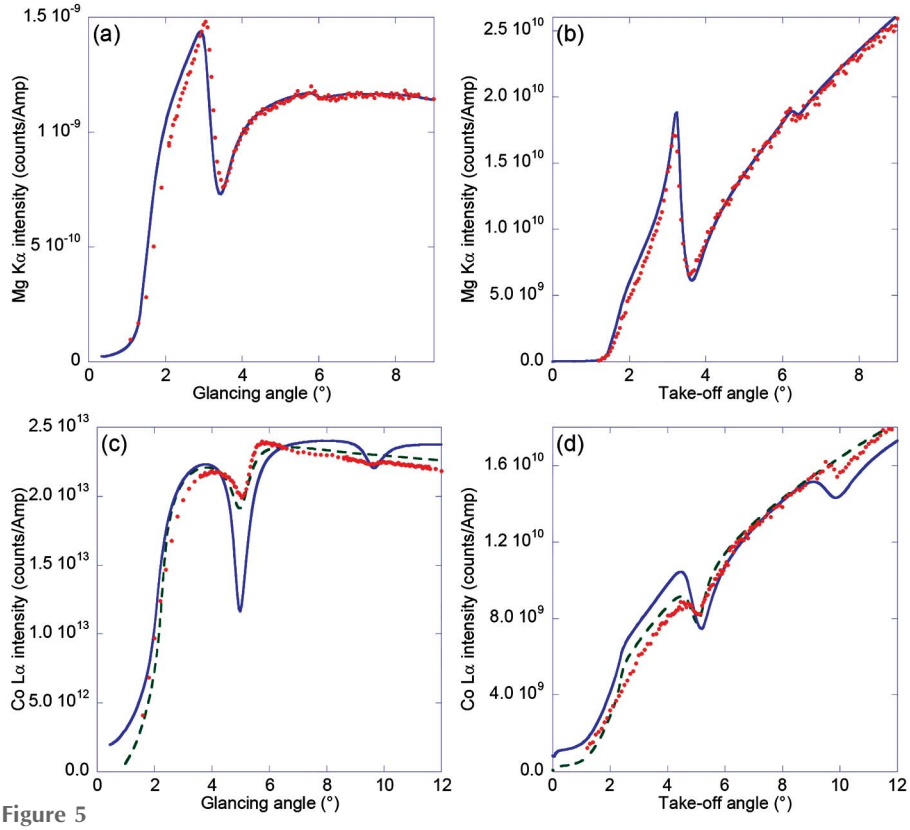

Figure 5
GI-XRF (*a*, *c*) and GE-XRF (*b*, *d*) curves for the Mg $K\alpha$ (*a*, *b*) and Co $L\alpha$ (*c*, *d*) emissions of the Mg/Zr/Co multilayer: dots, experiment; solid line: fit with a tri-layer stack; dashed line: fit with a bi-layer stack.

nuclear magnetic resonance and X-ray emission spectroscopies giving the chemical state of the Co and Mg atoms in the stack, respectively.

The analysis of the Co $L\alpha$ emission is more complicated. First, it must be kept in mind that the emission energy, 776.4 eV (Jonnard & Bonnelle, 2011), is only 2.4 eV away from the Co $2p_{3/2}$ ionization threshold, 778.8 eV (Jonnard & Bonnelle, 2011). That is to say, the Co optical constants used in the simulations have to be chosen in a range where they are strongly varying and also not known with high accuracy. This introduced an uncertainty on the fit of the angular curves. This is in contrast to the case of the Mg $K\alpha$ emission, where the emission energy, 1253.6 eV (Jonnard & Bonnelle, 2011), is about 50 eV lower than the Mg 1s ionization threshold, 1303.4 eV (Jonnard & Bonnelle, 2011).

For the Co $L\alpha$ emission of the Mg/Co/Zr system, the simulations reproduce the general shape of the GI and GE curves. These simulations are performed with starting parameters deduced from the reflectivity measurements, the optical indices of the CXRO database (http://henke.lbl.gov/optical_constants/) and assuming a stack without inter-diffusion at the interfaces, that is to say by using a tri-layer stack. For the Mg/Zr/Co system this description fails even to reproduce the contrast of the features, see Figs. 5(c) and 5(d). Keeping a tri-layer structure but allowing variation of the Co optical constants, the agreement between experimental and calculated emission curves is still not satisfactory. As a consequence, we modify Mg/Zr/Co as a Mg/Co_xZr_y bi-layer stack, where x and y are the relative numbers of Co and Zr atoms, respectively. The values of x and y, estimated from the number of Co and Zr atoms introduced within the Co and Zr layers in Mg/Zr/Co during its deposition, are found to be equal to 0.78 and 0.22, respectively, so that x/y is equal to 3.5. Such values are close to those of the $Co_{23}Zr_6$ compound present in the Zr–Co binary phase diagram (Predel, 1991). The simulations performed by modeling the stack as a Mg/Co_xZr_y bi-layer greatly improve the agreement with the experiment, see Figs. 5(c) and 5(d). A bi-layer stack of the same composition has already been used to fit the extreme UV reflectivity curves of a similar system, however with much thicker Mg layers (13 nm), designed to work around 25 nm (Le Guen *et al.*, 2011*a*). Let us note that regarding the Mg $K\alpha$ curve, there is no significant difference between the simulations with a tri- or bi-layer system, as the Mg atoms are not involved in interfacial diffusion.

Table 2
Elemental values of $\emptyset^*$, n_{WS} and V for calculating the mixing enthalpies of the Co–Mg, Co–Zr, Zr–Mg systems.

Element	$\emptyset^*$ (V)	$n_{WS}^{1/3}$ (d.u.)$^{1/3}$	V (cm^3 mol^{-1})
Mg	3.42	1.20	13.97
Co	5.10	1.77	6.70
Zr	3.62	1.38	14.10

Thus, the large differences between the curves of Mg/Co/Zr and Mg/Zr/Co allow us to deduce that the Zr-on-Co interfaces in the Mg/Co/Zr multilayer are abrupt, whereas the Co-on-Zr interfaces in the Mg/Zr/Co multilayer are wide enough to consider the two Co and Zr layers as a single layer. Generally, alternate interfaces in a multilayer structure are asymmetric due to the difference in the surface free energy of the constituents of the multilayer. This is analogous to what happens in the particularly well documented case for the Mo/Si system (Yulin *et al.*, 2002).

In order to understand the interfacial behavior of the Mg/Zr/Co system, we calculated the mixing enthalpies of the Co–Mg, Co–Zr and Mg–Zr systems by using Miedema's 'macroscopic atom' model, whose details are given elsewhere (Miedema *et al.*, 1980; Das *et al.*, 2013). This approach has already proved useful for explaining the interfacial phenomena taking place in annealed Co/Mo_2C nanometer multilayers (Yuan *et al.*, 2015). The parameters used for the calculations, the electronegativities $\emptyset^*$, the electron densities at the first Wigner–Seitz boundary n_{WS} and the atomic volumes V, are given in Table 2.

We show in Fig. 7 the calculated mixing enthalpies as a function of the mole fraction. The Co–Zr system shows a negative mixing enthalpy over the whole composition range, whereas the Co–Mg and Mg–Zr systems both show only positive values. This indicates that a compound is easy to form at the interfaces between the Co and Zr layers, which is not possible at the interfaces involving the Mg layers. Moreover, there is a large difference in the surface free energies of Co and Zr, 2.0 J m^{-2} and 1.6 J m^{-2}, respectively (Vitos *et al.*, 1998). Thus, during the deposition of the Co atoms on the Zr layers, because the surface free energy of Zr is lower, Co atoms can move on the surface guided by the chemical driving force. This leads to a strong mixing at the interfaces and to the formation of the Co_xZr_y compound in the Mg/Zr/Co multilayer. On the other hand, in the Mg/Co/Zr multilayer, during the deposition of the Zr atoms

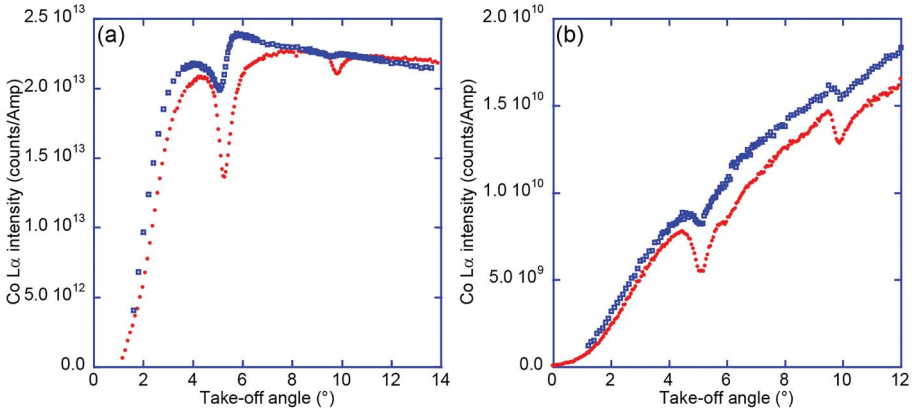

Figure 6
GI-XRF (a) and GE-XRF (b) curves for the Co $L\alpha$ emission of the Mg/Co/Zr (full dots) and Mg/Zr/Co (empty dots) multilayers.

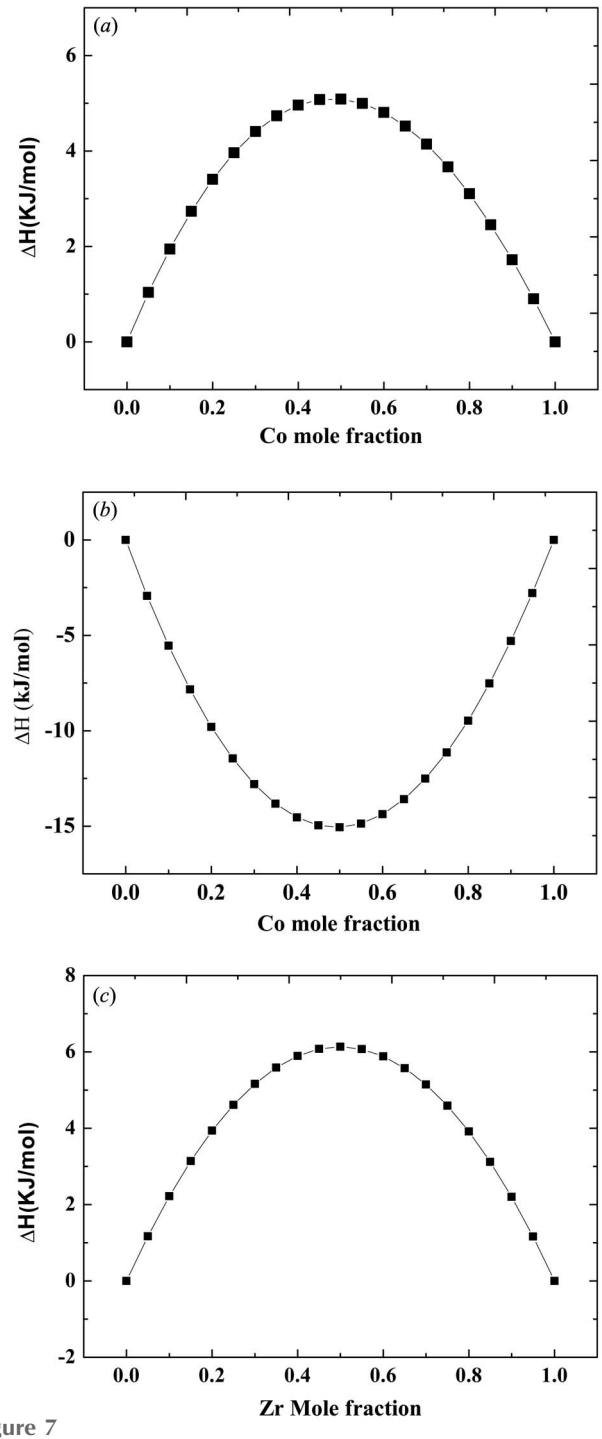

Figure 7
Calculated mixing enthalpies of the Co–Mg (*a*), Co–Zr (*b*) and Zr–Mg (*c*) systems.

onto the Co layers, no such chemical driving force exists. Therefore, the intermixing at the Zr-on-Co interface takes place as a result of random thermal motions only and, hence, the concentration profile is expected to be an abrupt error function. This is consistent with previous results (Le Guen *et al.*, 2011*a*,*b*; Zhu *et al.*, 2011) on large-period samples, demonstrating the good optical performances of Mg/Co/Zr owing to abrupt interfaces, whereas it was shown that Mg/Zr/Co has to be considered as a bi-layer system Mg/Co_xZr_y.

4. Conclusion

Whereas the reflectivity measurement in the hard X-ray range was not sensitive enough to detect the asymmetric behavior of interfaces in periodic multilayers, XRF generated by soft X-ray standing waves, in particular after the improvement of the angular resolution, prove useful to study the structure of periodic multilayer stacks and to characterize their buried interfaces in a non-destructive way. The combination of both GI and GE modes enables higher constraints to be put on the fitting parameters of the XSW curves. Working in the soft X-ray range gives sensitivity to the chemical state of the atoms owing to the large variation of the absorption coefficient in the vicinity of an absorption edge. Thus, the contrast of the XSW curves depends on the chemical state of the emitting element, *i.e.* to the element which is bound to the emitting element. This enables the depth sensitivity of the XSW technique to be coupled with the elemental and chemical sensitivity of XRF. Also, let us remark that photon excitation is not mandatory in the GE mode. In this case, XSW intensity measurements can be also made upon electron or ion irradiation, thus do not require a synchrotron facility.

The combination of GI- and GE-XRF generated by XSW allows us to determine that Mg/Co/Zr and Mg/Zr/Co multilayers have to be considered as tri-layer and bi-layer stacks, respectively, owing to the asymmetric behavior of the Zr-on-Co and Co-on-Zr interfaces following the positive mixing enthalpy of the Co–Zr system and the different values of the surface free energies of Co and Zr. Thus the Mg/Zr/Co multilayer can be described as Mg/Co_xZr_y with x/y around 3.5.

Acknowledgements

Some of this work was carried out in the framework of the international ANR-NSFC COBMUL project (ANR #10-INTB-902-01 and NSFC #11061130549) and of the Cai Yuanpei Project (EGIDE PHC No. 30248NF), 973 program (No. 2011CB922203), and National Natural Science Foundation of China (Nos. 11375131 and 11305104). A part of the research leading to these results has received funding from the European Community's Seventh Framework Programme (FP7/2007-2013) CALIPSO under grant agreement No. 312284.

References

Attwood, D. (2000). *Soft X-rays and Extreme Ultraviolet Radiation.* Cambridge University Press.
Bedzyk, M. J. & Libera, J. A. (2013). *The X-ray Standing Wave Technique*, pp. 122–131. Singapore: World Scientific.
Chauvineau, J.-P. & Bridou, F. (1996). *J. Phys. IV*, **06**, C53–C64.
Das, N., Mittra, J., Murty, B. S., Pabi, S. K., Kulkarni, U. D. & Dey, G. K. (2013). *J. Alloys Compd.* **550**, 483–495.
James, R. W. (1962). *The Optical Principle of the Diffraction of X-rays.* London: G. Bell & Sons.
Jonnard, P. & Bonnelle, C. (2011). *X-ray Spectrom.* **40**, 12–16.

Jonnard, P., Wang, Z.-S., Zhu, J.-T., Meny, C., André, J.-M., Hu, M.-H. & Le Guen, K. (2013). *Chin. Opt. Lett.* **11**, S10601.
Jonnard, P., Yuan, Y.-Y., Le Guen, K., André, J.-M., Zhu, J.-T., Wang, Z.-S. & Bridou, F. (2014). *J. Phys. B*, **47**, 165601.
Le Guen, K., Hu, M.-H., André, J.-M., Jonnard, P., Zhou, S. K., Li, H. C., Zhu, J. T., Wang, Z. S., Mahne, N., Giglia, A. & Nannarone, S. (2011*a*). *Appl. Phys. A*, **102**, 69–77.
Le Guen, K., Hu, M.-H., André, J.-M., Zhou, S. K., Li, H. C., Zhu, J. T., Wang, Z. S., Meny, C., Galtayries, A. & Jonnard, P. (2011*b*). *Appl. Phys. Lett.* **98**, 251909.
Li, W., Zhu, J., Ma, X., Li, H., Wang, H., Sawhney, K. J. S. & Wang, Z. (2012). *Rev. Sci. Instrum.* **83**, 053114.
Miedema, A. R., de Châtel, P. F. & de Boer, F. R. (1980). *Physica B + C*, **100**, 1–28.
Nannarone, S., Borgatti, F., DeLuisa, A., Doyle, B. P., Gazzadi, G. C., Giglia, A., Finetti, P., Mahne, N., Pasquali, L., Pedio, M., Selvaggi, G., Naletto, G., Pelizzo, M. G. & Tondello, G. (2004). *AIP Conf. Proc.* **705**, 450–453.
Predel, B. (1991). *Phase Equilibria, Crystallographic and Thermodynamic Data of Binary Alloys*, Vol. 5, edited by O. Madelung, Landolt-Börnstein, New Series, Group IV.
Sakata, O. & Jach, T. (2013). *The X-ray Standing Wave Technique*, pp. 108–121. Singapore: World Scientific.
Vitos, L., Ruban, A. V., Skriver, H. L. & Kollár, J. (1998). *Surf. Sci.* **411**, 186–202.
Von Laue, M. (1935). *Ann. Phys.* **415**, 705–746.
Yuan, Y., Le Guen, K., André, J.-M., Mény, C., Ulhaq, C., Galtayries, A., Zhu, J., Wang, Z. & Jonnard, P. (2015). *Appl. Surf. Sci.* **331**, 8–16.
Yulin, S., Feigl, T., Kuhlmann, T., Kaiser, N., Fedorenko, A. I., Kondratenko, V. V., Poltseva, O. V., Sevryukova, V. A., Zolotaryov, A. Y. & Zubarev, E. N. (2002). *J. Appl. Phys.* **92**, 1216–1220.
Zhu, J., Zhou, S., Li, H., Wang, Z., Jonnard, P., Le Guen, K., Hu, M.-H., André, J.-M., Zhou, H. & Huo, T. (2011). *Opt. Express*, **19**, 21849–21854.